

A Study of the Fourth-Order Small Perturbation Method for Scattering From Two-Layer Rough Surfaces

Metin A. Demir, Joel T. Johnson, *Fellow, IEEE*, and Tom J. Zajdel, *Student Member, IEEE*

Abstract—Predictions of the fourth-order small perturbation method (SPM) are examined for scattering from two rough surfaces in a layered geometry. Cross-polarized backscatter, in particular, is emphasized because use of the fourth-order SPM is required to obtain this quantity. The formulation of the SPM fields and incoherent ensemble-averaged normalized radar cross sections (NRCSs) up to the third and the fourth order in surface rms heights, respectively, are reviewed. It is shown that the fourth-order NRCS includes distinct contributions from upper and lower interface roughnesses, as well as an “interaction” term that couples the upper and lower interface roughnesses. A comparison with NRCS values computed using the “numerically exact” method of moments in the full bistatic scattering pattern is shown for verification, and NRCS values at the second and the fourth order are compared in order to assess the convergence of the SPM series. Although the number of parameters inherent in the two-layer rough surface scattering problem makes an exhaustive study of scattering effects difficult, several illustrative examples are presented to capture a range of scattering behaviors. The results emphasize the importance of interactions between the rough surfaces in producing cross-polarized backscattering and also indicate an increased significance of fourth-order contributions in the two-layer geometry as compared to the single-layer case.

Index Terms—Layered media, remote sensing, rough surface scattering.

I. INTRODUCTION

SEVERAL recent works [1]–[20] have examined the theory of scattering from two rough surfaces in a layered geometry (see Fig. 1). This problem is of interest due to its applications in the remote sensing of soil moisture, sea ice, and other geophysical effects as well as applications in optics. A variety of methods for predicting scattering have been explored, including both approximate [1]–[14] and numerically exact [15]–[20] approaches. For randomly rough surfaces, approximate methods (within their limits of applicability) have the

Manuscript received October 3, 2011; revised November 26, 2011; accepted December 23, 2011. Date of publication February 10, 2012; date of current version August 22, 2012.

M. A. Demir is with Department of Electrical and Computer Engineering, Istanbul Aydin University, Istanbul, Turkey (e-mail: metinaytekindemir@yahoo.com).

J. T. Johnson and T. J. Zajdel are with the Department of Electrical and Computer Engineering and ElectroScience Laboratory, The Ohio State University, Columbus, OH 43212 USA (e-mail: johnson@ece.osu.edu; tjzajdel@gmail.com).

Color versions of one or more of the figures in this paper are available online at <http://ieeexplore.ieee.org>.

Digital Object Identifier 10.1109/TGRS.2011.2182614

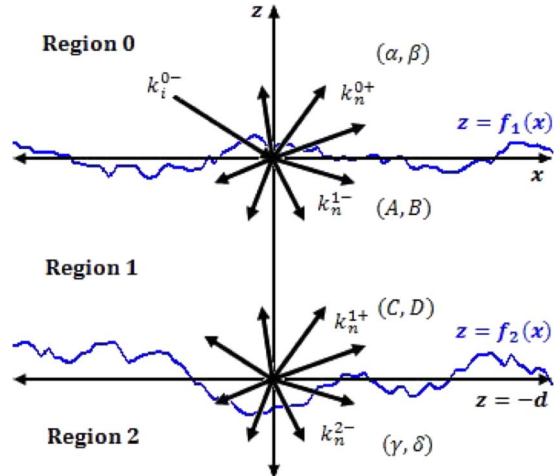


Fig. 1. Cross section of the two-layer geometry. The unknown field coefficients $\{\alpha, \beta, A, B, C, D, \gamma, \delta\}$ are labeled in their corresponding domains.

advantage of producing analytically averaged results, making them much more computationally efficient than the Monte Carlo simulations required with numerical methods. The analytical methods that have been reported include the small perturbation method (SPM) [1]–[7], geometrical optics (GO) approximation [8]–[10], the small-slope approximation [11], the “full-wave” method [12], and the integral equation method [13], [14].

Many geophysical cases of interest for layered rough surface geometries involve the use of lower microwave frequencies; this is because only at such frequencies will sufficient penetration occur to enable the observation of the lower interface. The use of the SPM is motivated in such cases because the inherent assumption of small surface height compared to the observing wavelength becomes more applicable at lower frequencies. It remains necessary that the surface slopes are small parameters comparable to or smaller than the ratio of the surface height to the electromagnetic wavelength.

The SPM produces a series expansion in surface heights for scattered fields. Among the previous studies utilizing the SPM for a two-layer geometry [1]–[7], the majority have utilized only the first-order terms in the series; only [1]–[3] have included higher order corrections. Generally, the first-order terms should dominate scattered fields when the SPM is applicable, so that utility of higher order corrections is limited in many situations. However, for some quantities of interest (such as

cross-polarized backscattering), first-order terms vanish, and higher order terms are needed to obtain a nonzero prediction [21]. An examination of higher order terms can also provide insight into the accuracy of the first-order solution. Although not considered in this paper, higher order corrections to the coherent reflection coefficient are also necessary in studies of thermal emission [22].

This paper examines higher order SPM corrections in the two-layer problem in an attempt to provide some insight into their properties, particularly with regard to cross-polarized backscatter. Field solutions up to the third order in surface height are used to enable the evaluation of the ensemble-averaged incoherent normalized radar cross section (NRCS) to the fourth order; note that fourth-order field corrections to the coherent reflection coefficient [25] are not considered in what follows. It is shown that the fourth-order incoherent NRCS correction includes distinct contributions from the upper and lower interface roughnesses, as well as an “interaction” term that couples both interface roughnesses. This interaction term is found to make significant contributions to cross-polarized backscatter returns. While the large number of parameters in the two-layer geometry makes a complete examination difficult, several example cases are used to illustrate some of the scattering effects that can occur.

The next section provides a brief review of the SPM solution for field quantities, and Section III discusses the corresponding NRCS evaluation. Section IV then presents a comparison of SPM predictions in one geometry with those of a numerical method for validation purposes. The comparisons shown are for the full hemispherical bistatic scattering pattern of the two-layer geometry considered. Further examinations of the influence of various parameters on backscattering, including surface roughness, layer thickness, incidence angle, and layer dielectric properties, are then reported in Section V.

II. REVIEW OF SPM SOLUTION FOR SCATTERED FIELDS

The SPM solution for the two-layer geometry was implemented following the one-layer solution originally developed by Rice [23] and later extended to the third [24] and higher [25] orders. Only an overview of the third-order two-layer solution is provided here; the full formulation including a recursive solution for arbitrary order is available in [3].

The two-layer geometry of Fig. 1 includes interfaces one ($z_1 = f_1(x, y)$) and two ($z_2 = -d + f_2(x, y)$) that separate three homogeneous regions $q = 0$ (the domain of excitation) to $q = 2$. As in [23]–[25], f_1 and f_2 are initially considered to be periodic functions with periods P_x and P_y in the x - and y -directions, respectively. The corresponding surface Fourier series coefficients at index $\bar{n}' = (n, m)$ are written as $h_{\bar{n}'}^{(1)}$ and $h_{\bar{n}'}^{(2)}$, respectively. The interfaces are assumed to be zero mean value so that $h_0^{(1)} = h_0^{(2)} = 0$.

Assuming plane wave incidence

$$\vec{E}_0^- = \hat{e}_i e^{i\vec{k}_0^0 \cdot \vec{r}} \quad (1)$$

the periodic surface assumption results in a discretization of scattered fields into Floquet mode series

$$\begin{aligned} \vec{E}_0^+ &= \sum_{\bar{n}} \left[\hat{h}_{\bar{n}} \alpha_{\bar{n}} + \hat{v}_{0+}^{\bar{n}} \beta_{\bar{n}} \right] e^{i\vec{k}_{\bar{n}}^0 \cdot \vec{r}} \\ \vec{E}_1^- &= \sum_{\bar{n}} \left[\hat{h}_{\bar{n}} A_{\bar{n}} + \hat{v}_{1-}^{\bar{n}} B_{\bar{n}} \right] e^{i\vec{k}_{\bar{n}}^1 \cdot \vec{r}} \\ \vec{E}_1^+ &= \sum_{\bar{n}} \left[\hat{h}_{\bar{n}} C_{\bar{n}} + \hat{v}_{1+}^{\bar{n}} D_{\bar{n}} \right] e^{i\vec{k}_{\bar{n}}^1 \cdot \vec{r}} \\ \vec{E}_2^- &= \sum_{\bar{n}} \left[\hat{h}_{\bar{n}} \gamma_{\bar{n}} + \hat{v}_{2-}^{\bar{n}} \delta_{\bar{n}} \right] e^{i\vec{k}_{\bar{n}}^2 \cdot \vec{r}} \end{aligned} \quad (2)$$

where an $e^{-i\omega t}$ time dependence is used. A (+) or a (−) superscript denotes upward or downward propagating waves (i.e., positive or negative \hat{z} components of the wave vector). Definitions of the polarization vectors $\hat{h}_{\bar{n}}$ and $\hat{v}_{q\pm}^{\bar{n}}$, propagation vectors $\vec{k}_{\bar{n}}^{q\pm}$, incident field polarization vectors \hat{e}_i , and magnetic fields corresponding to the aforementioned electric fields are provided in detail in [3, Ch. 3]. The goal of the SPM solution is to determine the complex amplitudes ($\alpha_{\bar{n}}$, $\beta_{\bar{n}}$, etc.) of the Floquet modes.

To simplify the notation, let $\varsigma_{\bar{n}}$ denote any of the complex amplitudes

$$\varsigma_{\bar{n}} = \{\alpha_{\bar{n}}, A_{\bar{n}}, C_{\bar{n}}, \gamma_{\bar{n}}, \beta_{\bar{n}}, B_{\bar{n}}, D_{\bar{n}}, \delta_{\bar{n}}\}. \quad (3)$$

The SPM solution procedure [3] provides the amplitudes $\varsigma_{\bar{n}}$ as a perturbation series in surface heights. At the zeroth order

$$\varsigma_{\bar{n}'}^{(0)} = \Gamma_{\varsigma} \tilde{\delta}_{\bar{n}'} \quad (4)$$

where $\tilde{\delta}_{\bar{n}'}$ denotes the Kronecker delta function. The zeroth-order field thus exists only in the specular direction ($\bar{n}' = 0$) having complex amplitudes Γ_{ς} corresponding to the flat-interface two-layer solution. At the first order

$$\varsigma_{\bar{n}'}^{(1)} = h_{\bar{n}'}^{(1)} g_{\varsigma}^{(1,0)}(\bar{n}') + h_{\bar{n}'}^{(2)} g_{\varsigma}^{(0,1)}(\bar{n}') \quad (5)$$

showing the “Bragg scattering” behavior of the first-order SPM but, in this case, involving contributions from both interfaces weighted by “kernel” functions $g_{\varsigma}^{(a,b)}(\bar{n}')$ that depend on the region permittivities, layer depth, and incidence and scattering angles. At the second order

$$\begin{aligned} \varsigma_{\bar{n}'}^{(2)} = & \sum_{\bar{n}_1} \left(h_{\bar{n}_1}^{(1)} h_{\bar{n}'-\bar{n}_1}^{(1)} g_{\varsigma}^{(2,0)}(\bar{n}', \bar{n}_1) \right. \\ & + h_{\bar{n}_1}^{(2)} h_{\bar{n}'-\bar{n}_1}^{(1)} g_{\varsigma}^{(1,1)}(\bar{n}', \bar{n}_1) \\ & \left. + h_{\bar{n}_1}^{(2)} h_{\bar{n}'-\bar{n}_1}^{(2)} g_{\varsigma}^{(0,2)}(\bar{n}', \bar{n}_1) \right) \end{aligned} \quad (6)$$

showing a sum of three terms with differing kernel functions. At the third order, a sum of four contributions is obtained

$$\begin{aligned} \varsigma_{\bar{n}'}^{(3)} = & \sum_{\bar{n}_1} \sum_{\bar{n}_2} \left(h_{\bar{n}_1}^{(1)} h_{\bar{n}_2}^{(1)} h_{\bar{n}'-\bar{n}_1-\bar{n}_2}^{(1)} g_{\varsigma}^{(3,0)}(\bar{n}', \bar{n}_1, \bar{n}_2) \right. \\ & + h_{\bar{n}_1}^{(2)} h_{\bar{n}_2}^{(1)} h_{\bar{n}'-\bar{n}_1-\bar{n}_2}^{(1)} g_{\varsigma}^{(2,1)}(\bar{n}', \bar{n}_1, \bar{n}_2) \\ & + h_{\bar{n}_1}^{(2)} h_{\bar{n}_2}^{(2)} h_{\bar{n}'-\bar{n}_1-\bar{n}_2}^{(1)} g_{\varsigma}^{(1,2)}(\bar{n}', \bar{n}_1, \bar{n}_2) \\ & \left. + h_{\bar{n}_1}^{(2)} h_{\bar{n}_2}^{(2)} h_{\bar{n}'-\bar{n}_1-\bar{n}_2}^{(2)} g_{\varsigma}^{(0,3)}(\bar{n}', \bar{n}_1, \bar{n}_2) \right). \end{aligned} \quad (7)$$

Note that both the second- and third-order field solutions include terms that depend only on the upper interface roughness, terms that depend only on the lower interface roughness, and terms that couple the two together.

III. NRCS EVALUATION

Ensemble-averaged NRCS values for an infinite surface are derived from the field perturbation series by considering the limit as the surface periods approach infinity [24]. The NRCS at a particular scattering angle [related to (\bar{n}')] and in a particular polarization can then be shown to be

$$\sigma_\zeta = \frac{K_\sigma^2 \langle |\zeta|^2 \rangle}{\delta k_x \delta k_y} \quad (8)$$

where $K_\sigma^2 = 4\pi k_0^2 \cos^2 \theta_s$ with θ_s being the polar angle of the scattered field and $k_0 = 2\pi/\lambda$ being the electromagnetic wavenumber in region zero. The quantities $\delta k_x = (2\pi/P_x)$ and $\delta k_y = (2\pi/P_y)$ are found to cancel when $\langle |h_{\bar{n}'}|^2 \rangle$ and other surface roughness properties are related to the continuous surface power spectral density.

It is assumed that surface roughness is described as a stationary Gaussian random process and that the roughness on the two interfaces is statistically independent. Note that some previous works have considered the case of correlated interfaces (e.g., [5]) in the first-order SPM, but such effects are outside the scope of this paper. The ensemble-averaged incoherent NRCS up to the fourth order in surface height is then a sum of the second- and fourth-order cross sections

$$\sigma_\zeta^{incoh} = \sigma_\zeta^{(2)} + \sigma_\zeta^{(4)} \quad (9)$$

where

$$\begin{aligned} \sigma_\zeta^{(2)} &= \sigma_\zeta^{10-10} + \sigma_\zeta^{01-01} \\ \sigma_\zeta^{(4)} &= \sigma_\zeta^{20-20} + \sigma_\zeta^{11-11} + \sigma_\zeta^{02-02} \\ &\quad + \sigma_\zeta^{10-30} + \sigma_\zeta^{01-03} + \sigma_\zeta^{10-12} + \sigma_\zeta^{01-21} \end{aligned} \quad (10)$$

with the superscripts $(ab - cd)$ denoting a and b upper and lower interface roughness terms, respectively, correlated with c and d upper and lower interface roughness terms. Note that the fourth-order correction to the NRCS can be either positive or negative; cases where the total NRCS is negative indicate that higher order SPM terms beyond the fourth order are required. No negative σ_ζ^{incoh} values occurred in the results to be shown.

Individual NRCS component contributions are

$$\sigma_\zeta^{10-10} = K_\sigma^2 W^{(1)}(\mathbf{k}_{\bar{n}'}) \left| g_\zeta^{(1,0)}(\mathbf{k}_{\bar{n}'}) \right|^2 \quad (11)$$

$$\sigma_\zeta^{01-01} = K_\sigma^2 W^{(2)}(\mathbf{k}_{\bar{n}'}) \left| g_\zeta^{(0,1)}(\mathbf{k}_{\bar{n}'}) \right|^2 \quad (12)$$

$$\begin{aligned} \sigma_\zeta^{20-20} &= K_\sigma^2 \iint d\mathbf{k}_{\bar{n}_1} W^{(1)}(\mathbf{k}_{\bar{n}_1}) W^{(1)}(\mathbf{k}_{\bar{n}'-\bar{n}_1}) \\ &\quad \times \left(\left| g_\zeta^{(2,0)}(\mathbf{k}_{\bar{n}'}, \mathbf{k}_{\bar{n}_1}) \right|^2 \right. \\ &\quad \left. + g_\zeta^{(2,0)*}(\mathbf{k}_{\bar{n}'}, \mathbf{k}_{\bar{n}'-\bar{n}_1}) g_\zeta^{(2,0)}(\mathbf{k}_{\bar{n}'}, \mathbf{k}_{\bar{n}_1}) \right) \end{aligned} \quad (13)$$

$$\begin{aligned} \sigma_\zeta^{11-11} &= K_\sigma^2 \iint d\mathbf{k}_{\bar{n}_1} W^{(2)}(\mathbf{k}_{\bar{n}_1}) W^{(1)}(\mathbf{k}_{\bar{n}'-\bar{n}_1}) \\ &\quad \times \left| g_\zeta^{(1,1)}(\mathbf{k}_{\bar{n}'}, \mathbf{k}_{\bar{n}_1}) \right|^2 \end{aligned} \quad (14)$$

$$\begin{aligned} \sigma_\zeta^{02-02} &= K_\sigma^2 \iint d\mathbf{k}_{\bar{n}_1} W^{(2)}(\mathbf{k}_{\bar{n}_1}) W^{(2)}(\mathbf{k}_{\bar{n}'-\bar{n}_1}) \\ &\quad \times \left(\left| g_\zeta^{(0,2)}(\mathbf{k}_{\bar{n}'}, \mathbf{k}_{\bar{n}_1}) \right|^2 \right. \\ &\quad \left. + g_\zeta^{(0,2)*}(\mathbf{k}_{\bar{n}'}, \mathbf{k}_{\bar{n}'-\bar{n}_1}) g_\zeta^{(0,2)}(\mathbf{k}_{\bar{n}'}, \mathbf{k}_{\bar{n}_1}) \right) \end{aligned} \quad (15)$$

$$\begin{aligned} \sigma_\zeta^{10-30} &= 2\text{Re} \left\{ K_\sigma^2 W^{(1)}(\mathbf{k}_{\bar{n}'}) g_\zeta^{(1,0)*}(\mathbf{k}_{\bar{n}'}) \right. \\ &\quad \times \iint d\mathbf{k}_{\bar{n}_1} W^{(1)} \\ &\quad \times (\mathbf{k}_{\bar{n}_1}) \left(g_\zeta^{(3,0)}(\mathbf{k}_{\bar{n}'}, \mathbf{k}_{\bar{n}'}, \mathbf{k}_{\bar{n}_1}) \right. \\ &\quad \left. + g_\zeta^{(3,0)}(\mathbf{k}_{\bar{n}'}, \mathbf{k}_{\bar{n}_1}, \mathbf{k}_{\bar{n}'}) \right. \\ &\quad \left. + g_\zeta^{(3,0)}(\mathbf{k}_{\bar{n}'}, \mathbf{k}_{\bar{n}_1}, -\mathbf{k}_{\bar{n}_1}) \right) \right\} \end{aligned} \quad (16)$$

$$\begin{aligned} \sigma_\zeta^{10-12} &= 2\text{Re} \left\{ K_\sigma^2 W^{(1)}(\mathbf{k}_{\bar{n}'}) g_\zeta^{(1,0)*}(\mathbf{k}_{\bar{n}'}) \right. \\ &\quad \times \iint d\mathbf{k}_{\bar{n}_1} W^{(2)}(\mathbf{k}_{\bar{n}_1}) g_\zeta^{(1,2)} \\ &\quad \times (\mathbf{k}_{\bar{n}'}, \mathbf{k}_{\bar{n}_1}, -\mathbf{k}_{\bar{n}_1}) \left. \right\} \end{aligned} \quad (17)$$

$$\begin{aligned} \sigma_\zeta^{01-21} &= 2\text{Re} \left\{ K_\sigma^2 W^{(2)}(\mathbf{k}_{\bar{n}'}) g_\zeta^{(0,1)*}(\mathbf{k}_{\bar{n}'}) \right. \\ &\quad \times \iint d\mathbf{k}_{\bar{n}_1} W^{(1)}(\mathbf{k}_{\bar{n}_1}) g_\zeta^{(2,1)} \\ &\quad \times (\mathbf{k}_{\bar{n}'}, \mathbf{k}_{\bar{n}'}, \mathbf{k}_{\bar{n}_1}) \left. \right\} \end{aligned} \quad (18)$$

$$\begin{aligned} \sigma_\zeta^{01-03} &= 2\text{Re} \left\{ K_\sigma^2 W^{(2)}(\mathbf{k}_{\bar{n}'}) g_\zeta^{(0,1)*}(\mathbf{k}_{\bar{n}'}) \right. \\ &\quad \times \iint d\mathbf{k}_{\bar{n}_1} W^{(2)}(\mathbf{k}_{\bar{n}_1}) \\ &\quad \times \left(g_\zeta^{(0,3)}(\mathbf{k}_{\bar{n}'}, \mathbf{k}_{\bar{n}'}, \mathbf{k}_{\bar{n}_1}) \right. \\ &\quad \left. + g_\zeta^{(0,3)}(\mathbf{k}_{\bar{n}'}, \mathbf{k}_{\bar{n}_1}, \mathbf{k}_{\bar{n}'}) \right. \\ &\quad \left. + g_\zeta^{(0,3)}(\mathbf{k}_{\bar{n}'}, \mathbf{k}_{\bar{n}_1}, -\mathbf{k}_{\bar{n}_1}) \right) \right\} \end{aligned} \quad (19)$$

where $W^{(j)}(\mathbf{k}_{\bar{n}'})$ represents the power spectral density of the j th interface, assumed in the results shown to have an isotropic Gaussian form

$$W^{(j)}(k_\rho) = \frac{u_j^2 l_j^2}{4\pi} \exp \left(-\frac{k_\rho^2 l_j^2}{4} \right), \quad j = 1, 2 \quad (20)$$

for $k_\rho \neq 0$ and to be equal to zero for $k_\rho = 0$ (zero mean profile). Here, u_j and l_j represent the rms height and correlation length, respectively, of the j th interface. It is noted that natural surfaces are more typically described in terms of exponential or power-law spectral densities. The Gaussian form used here was

selected to simplify the numerical computations and because Gaussian correlation functions are often used as an initial benchmark for comparison with other surface types. Other power spectral densities will be considered in future work.

The integrations required in (13)–(19) are performed numerically in polar coordinates over a domain that extends from the origin to wavenumbers where the power spectral density $W^{(j)}(\mathbf{k}_{\tilde{n}_1})$ is negligible. Discretization tests showed that approximately 20 points in azimuth by 20 points per electromagnetic wavenumber (k_0) provided sufficient accuracy in the results to be shown.

The total NRCS can also be written as a sum of contributions that separate the upper surface, lower surface, and interaction effects

$$\sigma_{\zeta}^{incoh} = \sigma_{\zeta}^{upper} + \sigma_{\zeta}^{lower} + \sigma_{\zeta}^{inter} \quad (21)$$

where

$$\sigma_{\zeta}^{upper} = \sigma_{\zeta}^{10-10} + \sigma_{\zeta}^{20-20} + \sigma_{\zeta}^{10-30} \quad (22)$$

$$\sigma_{\zeta}^{lower} = \sigma_{\zeta}^{01-01} + \sigma_{\zeta}^{02-02} + \sigma_{\zeta}^{01-03} \quad (23)$$

$$\sigma_{\zeta}^{inter} = \sigma_{\zeta}^{11-11} + \sigma_{\zeta}^{10-12} + \sigma_{\zeta}^{01-21}. \quad (24)$$

“Upper,” “lower,” and “interaction” ratios are also defined as the ratio of these terms to the total cross section, e.g.,

$$r^{int} = \frac{\sigma_{\zeta}^{inter}}{\sigma_{\zeta}^{incoh}}. \quad (25)$$

These contribution ratios will be examined in Section V for cross-polarized backscatter. A similar “fourth-order ratio” $\sigma_{\zeta}^{(4)}/\sigma_{\zeta}^{incoh}$ is illustrated for co-polarized backscatter in order to assess SPM convergence.

In general, the relative importance of fourth-order terms will increase as rms heights increase. Because the power spectral densities in (11)–(19) are directly proportional to the corresponding surface height variances and there is no other surface rms height dependence, it is straightforward to scale individual NRCS contributions as surface rms heights are varied. For this reason, variations of surface rms heights are not considered in what follows.

For cross-polarized backscatter, (21) can be rewritten as

$$\sigma_{\zeta}^{incoh} = u_1^4 \tilde{\sigma}_{\zeta}^{upper} + u_2^4 \tilde{\sigma}_{\zeta}^{lower} + u_1^2 u_2^2 \tilde{\sigma}_{\zeta}^{inter} \quad (26)$$

$$= u_1^2 u_2^2 \left(\frac{u_1^2}{u_2^2} \tilde{\sigma}_{\zeta}^{upper} + \frac{u_2^2}{u_1^2} \tilde{\sigma}_{\zeta}^{lower} + \tilde{\sigma}_{\zeta}^{inter} \right) \quad (27)$$

where the $\tilde{\sigma}$ quantities are computed with all rms heights normalized to unity. This form clarifies the relative importance of the upper, lower, and interaction terms as the surface rms heights are varied. In particular, the interaction term is more likely to make significant contributions when the surface height variances are equal since, in that case, all terms in the series are weighted equally. However, the relative contributions of each term remain dependent on layer properties, interface correlation lengths, and the scattering geometry.

IV. COMPARISON WITH NUMERICAL METHOD

Because the derivation of the SPM kernel functions requires a great deal of algebra, it is important to verify that the resulting implementations are accurate. Several approaches were used for verification, including comparison with a numerical solution of the SPM equations. Once a verified code was available, a final verification and SPM accuracy test was performed by comparing SPM predictions with those of a “numerically exact” solution of the two-layer problem. The numerically exact method used was the method of moments (MOM) for a 3-D scattering problem (i.e., “2-D” surface profiles). The general formulation of the MOM method used is described in [26], and the implementation was extended to allow for the two-layer dielectric medium geometry of interest. A similar MOM approach was also used in previous studies [9], [10] to assess a GO method in the two-layer problem.

The MOM simulation used surface profiles of 16 by 16 electromagnetic wavelengths, discretized into 512 by 512 points on each interface. Because there are four field components discretized at each surface point (on each interface), the final solution involves approximately two million unknowns. An iterative solution of the MOM matrix equation is used, combined with a “canonical grid” acceleration of the matrix-vector multiply for coupling of unknowns on a single interface. Coupling between interfaces is implemented without acceleration in the current code and dominates the computation. A parallelized implementation of the cross-interface coupling using eight processors enabled solutions to be obtained in approximately 10 CPU hours (per incident polarization) for a single surface realization. A Monte Carlo simulation over 64 surface realizations was then achieved through the use of 512 processors (i.e., 64 groups of 8). Supercomputing resources at the Maui High Performance Computing Center [27] were used in the final computations.

One issue in the MOM computations is the use of a “tapered wave” incident field to reduce edge truncation effects. While the tapered wave achieves this goal, it effectively introduces an averaging of cross sections over a small range of scattering angles. This averaging is only of concern in situations where cross sections vary rapidly with angle. Cross-polarized backscatter in the plane of incidence is one such case: the tapered wave averages very small in-plane cross-polarization results with larger out-of-plane cross-polarized returns, resulting in increased MOM cross-polarized levels. Similar behaviors happen for the bistatic HH NRCS in the cross-plane ($\phi_s = 90^\circ$) for small height surfaces. These effects can be reduced by increasing the surface size simulated, but such increases were not possible given the limited CPU resources available for the results shown. Differences between MOM and SPM predictions in these cases should therefore not be taken as meaningful. It is noted that a recent paper has described a new method for eliminating the use of tapered wave illuminations [28], but this approach has yet to be extended to the two-layer problem.

The case used in the comparison had rms heights and correlation lengths of 0.02λ and 0.5λ , respectively, on both interfaces. The relative permittivities of regions 1 and 2 are $5.4 + i0.44$ and $11.27 + i1$, respectively, and the layer thickness is 0.2λ . NRCS values in the complete bistatic hemisphere were computed for incidence angle $\theta_i = 40^\circ$.

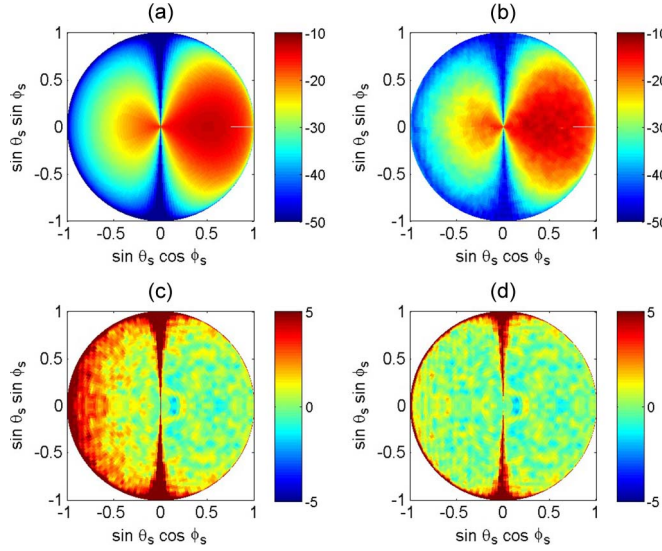


Fig. 2. Comparison of SPM and MOM bistatic scattering patterns: HH polarization. $u_1 = u_2 = 0.02\lambda$, $l_1 = l_2 = 0.5\lambda$, $\epsilon_1 = 5.4 + i0.44$, $\epsilon_2 = 11.27 + i$, $d = 0.2\lambda$, and $\theta_i = 40^\circ$.

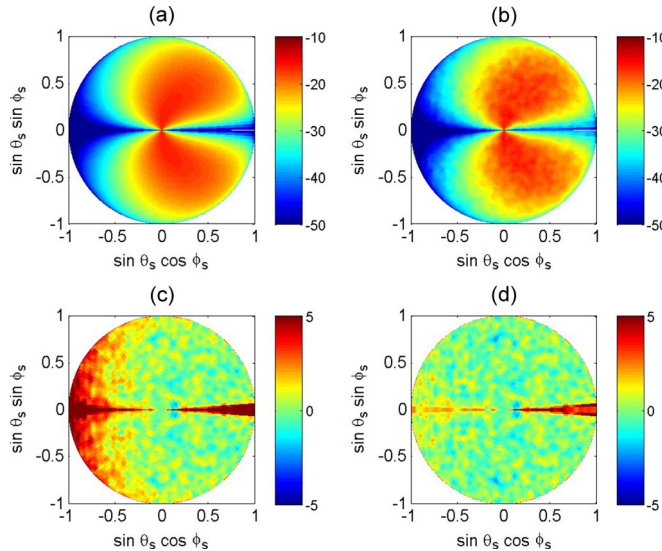


Fig. 3. Comparison of SPM and MOM bistatic scattering patterns for the configuration of Fig. 2: VH polarization.

Fig. 2 plots *HH* ensemble-averaged incoherent NRCS returns in decibels from the fourth-order SPM (upper left) and the MOM (upper right), as well as the difference between MOM and second-order SPM decibel values (lower left) and between MOM and fourth-order SPM decibel values (lower right). Similar plots for *VH* and *VV* polarizations are provided in Figs. 3 and 4; *HV* polarization is similar in most respects to *VH* and therefore was not plotted. The plot formats are a projection of the hemisphere onto a horizontal plane, in which the horizontal and vertical axes represent $\sin \theta_s \cos \phi_s$ and $\sin \theta_s \sin \phi_s$, respectively. The incident field approaches from the left along the horizontal axis so that the horizontal axis of the plot is the plane of incidence.

The results show typical behaviors for rough surface hemispherical scattering patterns in the small height limit, including larger co-pol returns in the specular region, small cross-pol

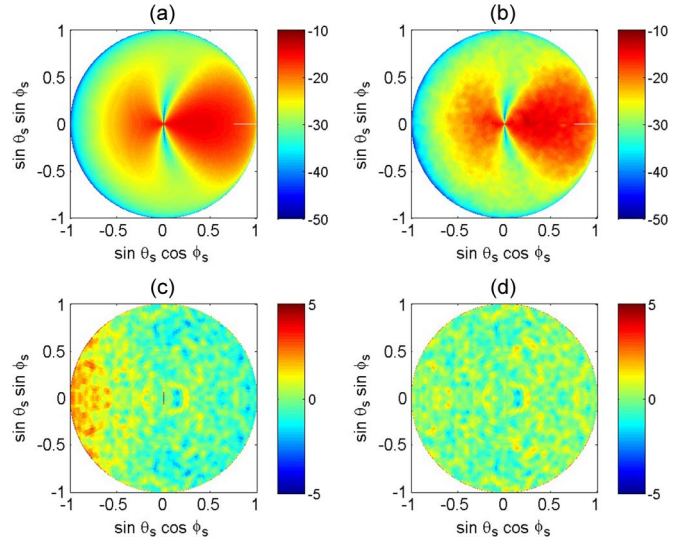


Fig. 4. Comparison of SPM and MOM bistatic scattering patterns for the configuration of Fig. 2: VV polarization.

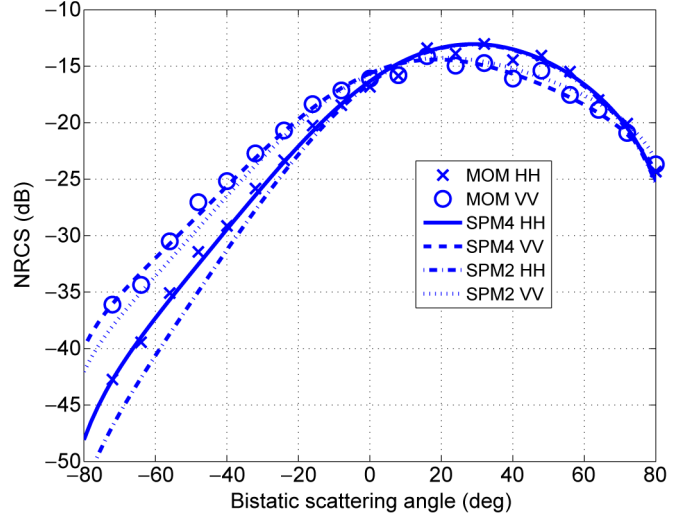


Fig. 5. Comparison of SPM and MOM in-plane bistatic scattering patterns for the configuration of Fig. 2.

returns in the plane of incidence, and small *HH* returns in the cross-plane ($\phi_s = 90^\circ$). Note that coherent scattering is removed from the MOM simulations so that only incoherent responses are compared. The ratio plots (illustrated in decibels) show larger differences in the small cross-sectional regions (as discussed previously) but otherwise show good agreement (with some speckle due to the finite number of MOM realizations) between the MOM and SPM in all polarizations. A reduction in differences between the SPM and MOM is also apparent when fourth-order contributions are included, particularly in the “backward” portion of the hemisphere (i.e., the second and third quadrants). These results show that the fourth-order SPM can make appreciable contributions to co-pol returns even for the relatively flat interfaces considered and that the fourth-order SPM is sufficient in this example.

Fig. 5 illustrates the same comparison for *HH* and *VV* returns in the plane of incidence and again shows a good

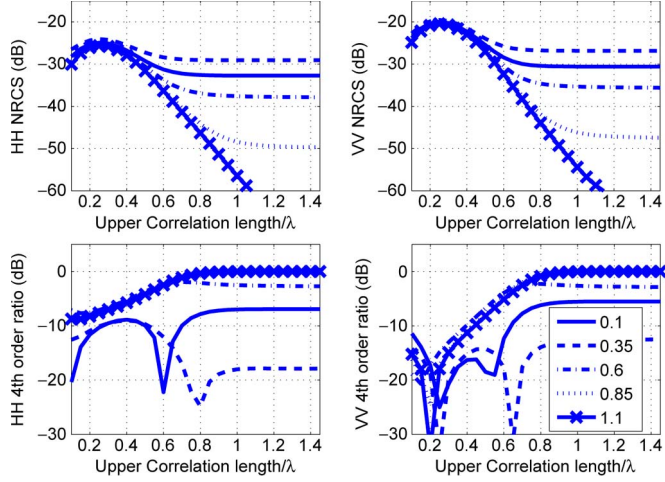


Fig. 6. Backscattered (upper left) HH and (upper right) VV NRCS at $\theta_i = 40^\circ$ as a function of upper surface correlation length (horizontal axis), with lower surface correlation length indicated in legend. Fourth-order ratios $\sigma_{\zeta}^{(4)}/\sigma_{\zeta}^{incoh}$ are also illustrated for (lower left) HH and (lower right) VV . $u_1 = u_2 = 0.02\lambda$, $\epsilon_1 = 5.4 + i0.44$, $\epsilon_2 = 11.27 + i$, and $d = 0.2\lambda$.

agreement between SPM and MOM predictions, as well as the significance of the fourth-order contribution at some angles.

V. INFLUENCE OF CORRELATION LENGTHS AND LAYER PROPERTIES ON BACKSCATTERING

A. Surface Correlation Lengths

Although the influence of surface rms height on individual SPM contributions is clear, changes in surface correlation lengths require recomputation of the fourth-order integrations (13)–(19). Generally, longer correlation length surfaces have narrower power spectral densities so that contributions from SPM kernel functions in the integration are more limited to regions near the origin in wavenumber space.

Fig. 6 plots the HH and the VV backscattered NRCS at $\theta_i = 40^\circ$, as well as the HH and VV fourth-order ratios, as a function of the upper and lower surface correlation lengths for the configuration of Figs. 2–5. A trend of reduced cross-sectional levels as the correlation lengths increase (i.e., “smoother” surfaces since surface rms heights are kept constant) is observed. Cross sections are observed to approach constant values for larger upper correlation lengths that depend on the correlation length of the lower interface. These behaviors reflect the fact that upper and lower interface terms are combined, with the rougher surface (i.e., smaller correlation length in this case) eventually dominating the total two-layer return. A contrary trend of increasing NRCS levels with correlation length occurs for very small correlation lengths, with a maximum achieved in this case around a correlation length of 0.25 wavelengths. This maximum is associated with the dependence of the surface power spectral density on correlation length (20).

Fourth-order co-pol ratios in Fig. 6 show that fourth-order contributions are relatively weak for the shorter correlation lengths but become more important when both interface correlation lengths are large (where total second-order contributions become small). Because the fourth-order contribution can be

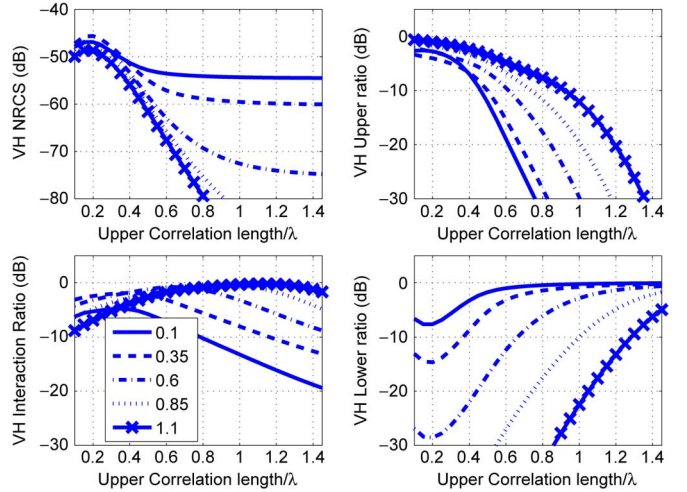


Fig. 7. Backscattered (upper left) VH NRCS at $\theta_i = 40^\circ$ as a function of upper surface correlation length (horizontal axis), with lower surface correlation length indicated in legend. (Upper right) Upper, (lower left) interaction, and (lower right) lower contribution ratios are also illustrated. $u_1 = u_2 = 0.02\lambda$, $\epsilon_1 = 5.4 + i0.44$, $\epsilon_2 = 11.27 + i$, and $d = 0.2\lambda$.

positive or negative, rapid decreases are observed on the decibel scale used when a sign change of the fourth order contribution occurs.

The influence of surface correlation lengths on cross-polarized backscatter is illustrated in Fig. 7, which includes the total VH NRCS as well as the upper, lower, and interaction ratios, defined as in (25). Cross-pol total NRCS levels are very low but would increase as rms height to the fourth power for rougher surfaces. Similar behaviors are observed for the total NRCS as in the co-pol cases. Upper interface contributions dominate the total return at smaller upper interface correlation lengths, but interaction effects make significant contributions as the upper correlation length increases. Lower interface contributions are more significant in cases with a very smooth upper interface. Note that interaction effects account for less than 10% of the total cross-pol return in this case only when the upper surface is very smooth and the lower one is very rough. When both surfaces are smooth, interaction effects dominate the (small) cross-pol return.

B. Incidence Angle and Layer Depth

The preceding section considered backscattering at 40° incidence angle at a fixed layer depth of 0.2λ . Fig. 8 plots HH and VV NRCS values and fourth-order ratios for backscattering as a function of incidence angle, with the layer depth (in wavelengths) as a parameter. The results show typical decreasing backscatter returns with incidence angle, with only a small influence of layer depth for these layer properties. Fourth-order ratios show an increasing importance of the fourth-order contribution at larger incidence angles (again where second-order SPM contributions are smaller), as well as an increased importance for thinner layers (consistent with increased attenuation in region one for thicker layers). Fourth-order contributions decrease NRCS levels at smaller incidence angles but increase them at larger angles, and the layer depth has a small effect on the location of the transition in sign.

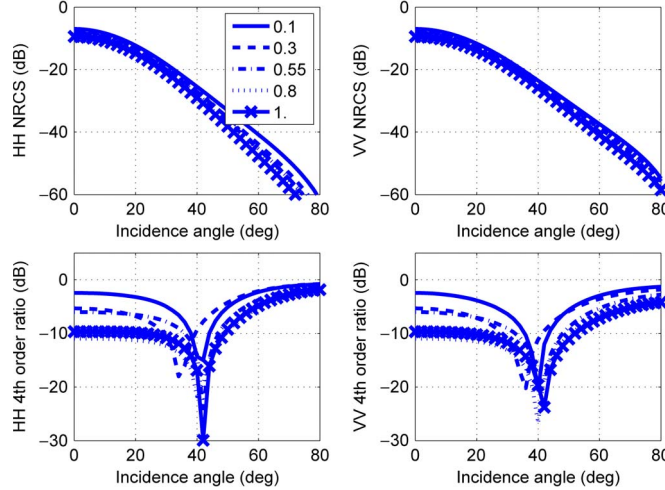


Fig. 8. Backscattered (upper left) HH and (upper right) VV NRCS as a function of incidence angle. Layer depth parameter indicated in legend. Fourth-order ratios for (lower left) HH and (lower right) VV are also plotted. $u_1 = u_2 = 0.02\lambda$, $l_1 = l_2 = 0.5\lambda$, $\epsilon_1 = 5.4 + i0.44$, and $\epsilon_2 = 11.27 + i$.

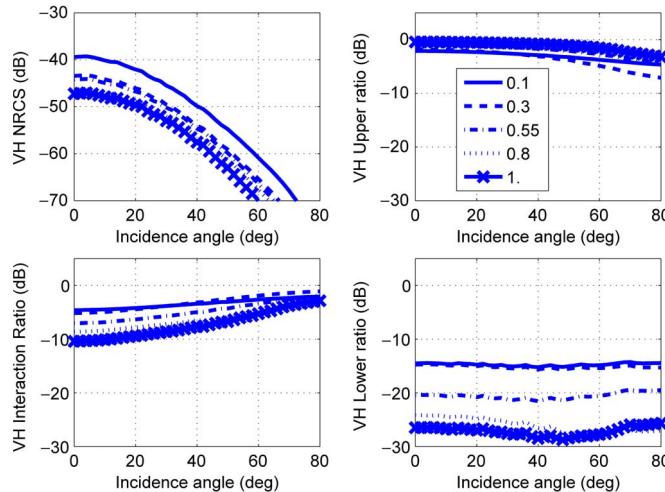


Fig. 9. Backscattered (upper left) VH NRCS returns for the configuration of Fig. 8 as a function of incidence angle, with layer depth indicated in legend. (Upper right) Upper, (lower left) interaction, and (lower right) lower contribution ratios are also illustrated.

Cross-pol variations are investigated in Fig. 9, again by plotting the total NRCS along with the upper, lower, and interaction ratios. The results again show decreasing HV returns with incidence angle, along with a moderate influence of the layer depth, with thinner layers providing larger returns. For the roughness properties and layer configuration considered, upper and interaction terms dominate lower surface contributions in all cases, and interaction effects become more significant at larger observation angles and smaller layer depths. Note that both interaction effects and lower surface returns are impacted by attenuation in region one.

A clearer examination of the influence of layer depth is provided in Fig. 10, which plots total HH , HV , and VV NRCS returns as a function of layer depth, with the incidence angle as a parameter. Oscillatory behaviors in NRCS are observed with layer depth at all incidence angles, even in the fourth-order cross-pol returns. These oscillations generally decrease with

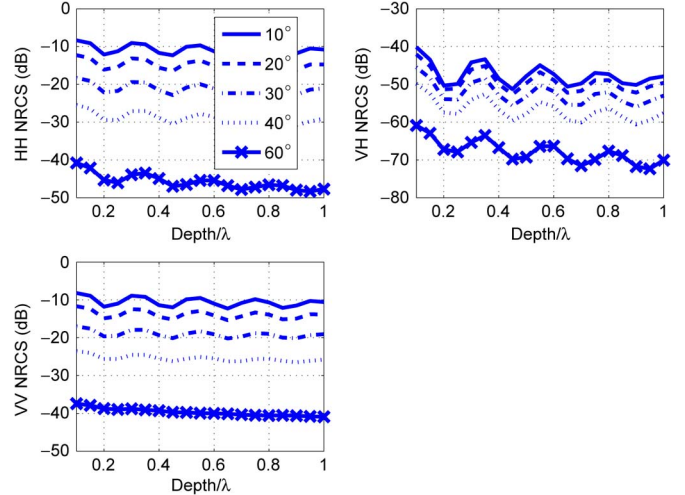


Fig. 10. Backscattered (upper left) HH , (upper right) VH , and (lower left) VV NRCS versus layer depth, with incidence angle as a parameter. $u_1 = u_2 = 0.02\lambda$, $l_1 = l_2 = 0.5\lambda$, $\epsilon_1 = 5.4 + i0.44$, and $\epsilon_2 = 11.27 + i$.

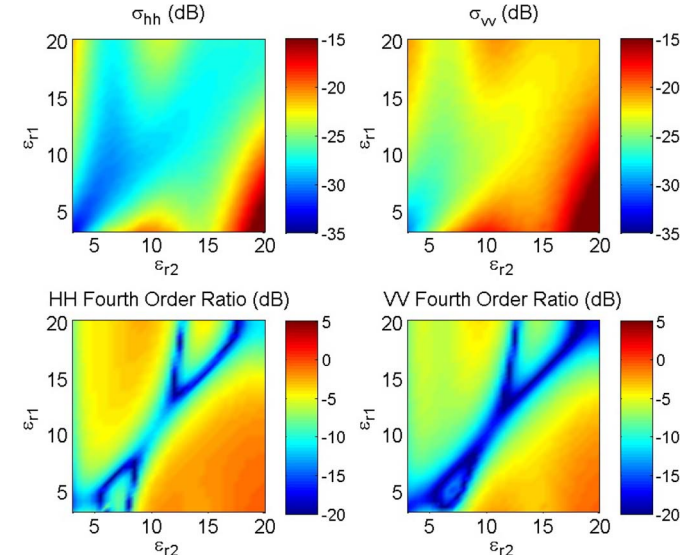


Fig. 11. Images of backscattered (upper left) HH and (upper right) VV NRCS at $\theta_i = 40^\circ$ as a function of the relative permittivities of regions one and two. Fourth-order ratios are also illustrated for (lower left) HH and (lower right) VV . $u_1 = u_2 = 0.02\lambda$, $l_1 = l_2 = 0.5\lambda$, and $d = 0.2\lambda$.

incidence angle due to increases in attenuation through region one at larger incidence angles. Properties of these oscillations strongly depend on the layered geometry investigated.

C. Effect of Dielectric Constants

The preceding examples have all utilized fixed dielectric constants in the layered geometry. Fig. 11 illustrates HH and VV NRCS returns and fourth-order ratios as the relative permittivities of regions one and two are varied over $3, 3.5, \dots, 20$ with zero imaginary parts in both regions. Backscattering at 40° is considered for a 0.2λ thick layer having equal rms heights and correlation lengths of 0.02λ and 0.5λ , respectively. Note that the case in which the two permittivities are equal (the lower-to-upper diagonal of the images shown) represents a single-layer case whose permittivity varies along the diagonal.

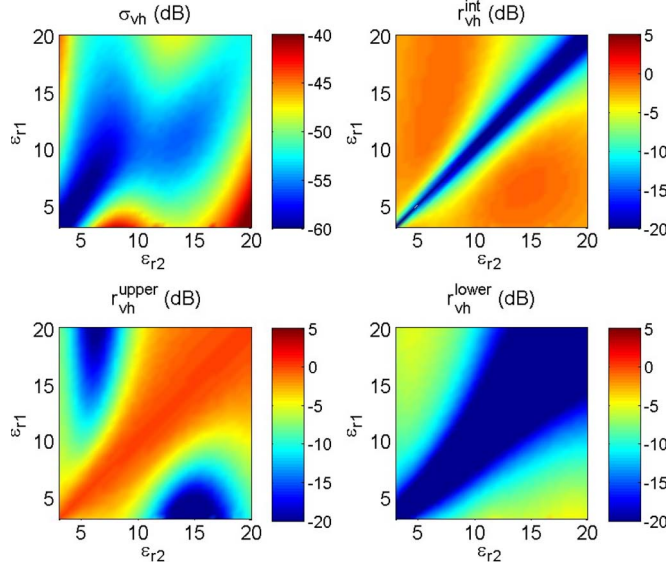


Fig. 12. Images of (upper left) backscattered VH NRCS and (lower left) upper, (upper right) interaction, and (lower right) lower contribution ratios at $\theta_i = 40^\circ$ as a function of the relative permittivities of regions one and two. $u_1 = u_2 = 0.02\lambda$, $l_1 = l_2 = 0.5\lambda$, and $d = 0.2\lambda$.

The results for this geometry show a complex variation with medium permittivities, with the largest co-pol returns occurring in the cases with a small permittivity layer overlying a larger permittivity medium. Fourth-order ratios are appreciable (> -10 dB) in all cases, with the exception of regions near the equal permittivity line (i.e., the single-layer case). In general, these results suggest that fourth-order contributions to co-pol returns can be more significant in the two-layer configuration than in the single-layer case.

Cross-pol NRCS results in Fig. 12 show complex variations similar to those observed for co-pol. Contributions to cross-pol returns from the interaction and lower contributions vanish identically along the image diagonal (the single-layer case), but interaction contributions are otherwise significant. Lower interface contributions for these roughness parameters are appreciable only in the cases with larger differences between the two region permittivities.

VI. CONCLUSION

The results of this paper demonstrate some of the possible scattering effects that can occur in the two-layer rough surface problem. Although a comprehensive evaluation of scattering in this problem is difficult due to the large number of parameters involved, the examples shown in Section V-C indicate that fourth-order contributions in the SPM model can be more significant in the two-layer problem than in the single layer case (note that the case considered had equal roughness statistics on both interfaces.) Properties of the cross-polarized backscatter, available only at the fourth or higher order in the SPM, also showed that interaction effects between the two surfaces can, in some cases, be the dominant contribution to cross-pol returns. The general behaviors of the results were consistent with an expectation of an increased influence of the rougher interface on total returns, as well as decreased influence of the lower in-

terface for cases with larger attenuation in region one. Because the computation of the fourth-order SPM requires only a set of double integrations for evaluation, it remains a reasonably efficient method for application in data analysis and mission planning for systems involving two-layer geometries.

Convergence of the SPM series for the two-layer geometry should be expected to depend on properties of the surface roughness, layered media, and scattering geometry, as shown by the examples considered. While the accuracy of the fourth-order SPM was demonstrated for one small height example through a comparison with the MOM (see Section IV), it should generally be expected that the fourth-order SPM is applicable in cases where it produces a small-to-moderate correction of the second-order SPM solution. In the cases where the second-order SPM vanishes for a particular polarization (e.g., backscattered cross-polarization), it appears that applicability can still be established by examination of other polarizations for the same configuration (e.g., backscattered copolarization). More detailed assessments of SPM applicability will require further numerical studies beyond the scope of this paper or the evaluation of the next-order term in the SPM NRCS series (sixth order in power, requiring a fifth-order field solution for stationary Gaussian process surfaces).

ACKNOWLEDGMENT

The authors would like to thank the Maui High Performance Computing Center for the use of supercomputing resources and Prof. M. Moghaddam and X. Duan of the University of Michigan for technical discussions and code comparisons.

REFERENCES

- [1] A. Soubret, G. Berginc, and C. Bourrée, "Application of reduced Rayleigh equations to electromagnetic wave scattering by two-dimensional randomly rough surfaces," *Phys. Rev. B, Condens. Matter*, vol. 63, no. 24, p. 245411, 2001.
- [2] A. Soubret, G. Berginc, and C. Bourrée, "Backscattering enhancement of an electromagnetic wave scattered by two-dimensional rough layers," *J. Opt. Soc. Amer. A, Opt. Image Sci.*, vol. 18, no. 11, pp. 2778–2788, Nov. 2001.
- [3] M. A. Demir, "Perturbation theory of electromagnetic scattering from layered media with rough interfaces," Ph.D. dissertation, Ohio State Univ., Columbus, 2007.
- [4] I. M. Fuks and A. G. Voronovich, "Wave diffraction by rough interfaces in an arbitrary plane-layered medium," *Waves Random Media*, vol. 10, no. 2, pp. 253–272, 2000.
- [5] A. Tabatabaeenejad and M. Moghaddam, "Bistatic scattering from three-dimensional layered rough surfaces," *IEEE Trans. Geosci. Remote Sens.*, vol. 44, no. 8, pp. 2102–2114, Aug. 2006.
- [6] S. Afifi and R. Dusseaux, "On the co-polarized phase difference of rough layered surfaces: Formulae derived from the small perturbation method," *IEEE Trans. Antennas Propag.*, vol. 59, no. 7, pp. 2607–2618, Jul. 2011.
- [7] P. Imperatore, A. Iodice, and D. Riccio, "Physical meaning of perturbative solutions for scattering from and through multilayered structures with rough interfaces," *IEEE Trans. Antennas Propag.*, vol. 58, no. 8, pp. 2710–2724, Aug. 2010.
- [8] N. Pinel and C. Bourlier, "Scattering from very rough layers under the geometric optics approximation: Further investigation," *J. Opt. Soc. Amer. A, Opt. Image Sci.*, vol. 25, no. 6, pp. 1293–1306, Jun. 2008.
- [9] N. Pinel, J. Johnson, and C. Bourlier, "A geometrical optics model of three dimensional scattering from a rough surface over a planar surface," *IEEE Trans. Antennas Propag.*, vol. 57, no. 2, pp. 546–554, Feb. 2009.
- [10] N. Pinel, J. Johnson, and C. Bourlier, "A geometrical optics model of three dimensional scattering from a rough layer with two rough surfaces," *IEEE Trans. Antennas Propag.*, vol. 58, no. 3, pp. 809–816, Mar. 2010.

- [11] G. Berginc and C. Bourrelly, "The small-slope approximation method applied to a three dimensional slab with rough boundaries," *Progr. Elect. Res.*, vol. 73, pp. 131–211, 2007.
- [12] E. Bahar and Y. Zhang, "Diffuse like and cross-polarized fields scattered from irregular layered structures: Full-wave analysis," *IEEE Trans. Antennas Propag.*, vol. 47, no. 5, pp. 941–948, May 1999.
- [13] Y. Lasne, P. Paillou, T. August-Bernex, G. Ruffie, and G. Grandjean, "A phase signature for detecting wet subsurface structures using polarimetric L-band SAR," *IEEE Trans. Geosci. Remote Sens.*, vol. 42, no. 8, pp. 1683–1694, Aug. 2004.
- [14] Y. Lasne, P. Paillou, G. Ruffie, and M. Crapeau, "Effect of multiple scattering on the phase signature of wet subsurface structures: Applications to polarimetric L- and C-band SAR," *IEEE Trans. Geosci. Remote Sens.*, vol. 43, no. 8, pp. 1716–1726, Aug. 2005.
- [15] M. El-Shenawee, "Polarimetric scattering from two-layered two-dimensional random rough surfaces with and without buried objects," *IEEE Trans. Geosci. Remote Sens.*, vol. 42, no. 1, pp. 67–76, Jan. 2004.
- [16] C. D. Moss, T. M. Grzegorczyk, H. C. Han, and J. A. Kong, "Forward–backward method with spectral acceleration for scattering from layered rough surfaces," *IEEE Trans. Antennas Propag.*, vol. 54, no. 3, pp. 1006–1016, Mar. 2006.
- [17] C. Kuo and M. Moghaddam, "Electromagnetic scattering from multilayer rough surfaces with arbitrary dielectric profiles for remote sensing of subsurface soil moisture," *IEEE Trans. Geosci. Remote Sens.*, vol. 45, no. 2, pp. 349–366, Feb. 2007.
- [18] N. Deschamps and C. Bourlier, "Electromagnetic scattering from a rough layer: Propagation-inside-layer expansion method combined with forward–backward novel spectral acceleration," *IEEE Trans. Antennas Propag.*, vol. 55, no. 12, pp. 3576–3586, Dec. 2007.
- [19] X. Duan and M. Moghaddam, "3-D vector electromagnetic scattering from arbitrary random rough surfaces using stabilized extended boundary condition method for remote sensing of soil moisture," *IEEE Trans. Geosci. Remote Sens.*, vol. 50, no. 1, pp. 87–103, Jan. 2012.
- [20] X. Duan and M. Moghaddam, "Bistatic Vector 3D Scattering from Layered Rough Surfaces Using Stabilized Extended Boundary Condition Method," *Trans. Geosci. Remote Sens.*, 2012, submitted to publication.
- [21] G. R. Valenzuela, "Depolarization of EM waves by slightly rough surfaces," *IEEE Trans. Antennas Propag.*, vol. AP-15, no. 4, pp. 552–557, Jul. 1967.
- [22] J. T. Johnson, "Thermal emission from a layered medium bounded by a slightly rough interface," *IEEE Trans. Geosci. Remote Sens.*, vol. 39, no. 2, pp. 368–378, Feb. 2001.
- [23] S. O. Rice, "Reflection of electromagnetic waves from slightly rough surfaces," *Commun. Pure Appl. Math.*, vol. 4, no. 2/3, pp. 361–378, Aug. 1951.
- [24] J. T. Johnson, "Third order small perturbation method for scattering from dielectric rough surfaces," *J. Opt. Soc. Amer. A, Opt. Image Sci.*, vol. 16, no. 11, pp. 2720–2726, Nov. 1999.
- [25] M. A. Demir and J. T. Johnson, "Fourth and higher order small perturbation solution for scattering from dielectric rough surfaces," *J. Opt. Soc. Amer. A, Opt. Image Sci.*, vol. 20, no. 12, pp. 2330–2337, Dec. 2003.
- [26] J. T. Johnson and R. J. Burkholder, "Coupled canonical grid/discrete dipole approach for computing scattering from objects above or below a rough interface," *IEEE Trans. Geosci. Remote Sens.*, vol. 39, no. 6, pp. 1214–1220, Jun. 2001.
- [27] Maui High Performance Computing Center Website, 2011. [Online]. Available: <http://www.mhpcc.hpc.mil>
- [28] M. Saillard and G. Soriano, "Rough surface scattering at low grazing incidence: A dedicated model," *Radio Sci.*, vol. 46, p. RS0E13, 2011, doi: 10.1029/2010RS004641.

Metin A. Demir received the B.Sc. degrees in electrical engineering and applied mathematics from the Technical University of Istanbul, Istanbul, Turkey, in 2001 and the M.Sc. and Ph.D. degrees from The Ohio State University, Columbus, in 2003 and 2007, respectively.

He is currently an Assistant Professor in the Department of Electrical and Computer Engineering, Istanbul Aydin University, Istanbul. His research interests include computational electromagnetics, radar signal processing, and microwave remote sensing.

Joel T. Johnson (S'88–M'96–SM'03–F'09) received the Bachelor of Electrical Engineering degree from the Georgia Institute of Technology, Atlanta, in 1991 and the S.M. and Ph.D. degrees from the Massachusetts Institute of Technology, Cambridge, in 1993 and 1996, respectively.

He is currently a Professor with the Department of Electrical and Computer Engineering and ElectroScience Laboratory, The Ohio State University, Columbus. His research interests are in the areas of microwave remote sensing, propagation, and electromagnetic wave theory.

Dr. Johnson is a member of Commissions B and F of the International Union of Radio Science (URSI) and a member of Tau Beta Pi, Eta Kappa Nu, and Phi Kappa Phi. He was the recipient of the 1993 Best Paper Award from the IEEE Geoscience and Remote Sensing Society, was named an Office of Naval Research Young Investigator, National Science Foundation Career awardee, and Presidential Early Career Award for Scientists and Engineers (PECASE) recipient in 1997, and was recognized by the U.S. National Committee of URSI as a Booker Fellow in 2002.

Tom J. Zajdel (S'09) is currently working toward the B.S. degree in electrical and computer engineering at The Ohio State University, Columbus, and is to graduate in June 2012.

He is a Research Assistant with the Ohio State's Eye and Ear Institute, Columbus, and also serves as a Teaching Assistant for the Ohio State's Fundamentals of Engineering for Honors program, Columbus. His research interests are in the areas of biological signal processing, neuroscience, and electromagnetic wave theory.

Mr. Zajdel is a member of Eta Kappa Nu.